

A viscoelastic constitutive model for shape memory polymer composites: Micromechanical modeling, numerical implementation and application in 4D printing

Chengjun Zeng^a, Liwu Liu^a, Yunqiang Hu^a, Wenfeng Bian^b, Jinsong Leng^{c, **}, Yanju Liu^{a, *}

^a Department of Astronautical Science and Mechanics, Harbin Institute of Technology (HIT), No. 92 West Dazhi Street, PO Box 301, Harbin, 150001, People's Republic of China

^b Department of Civil Engineering, Harbin Institute of Technology (HIT), Weihai, 264209, People's Republic of China

^c Center for Composite Materials and Structures, Harbin Institute of Technology (HIT), No. 2 YiKuang Street, Harbin, 150080, People's Republic of China

ARTICLE INFO

Keywords:

Shape memory
Viscoelasticity
Interfacial damage
Constitutive model
4D printing

ABSTRACT

In this work, a novel micromechanics-based thermo-viscoelastic constitutive model for shape memory polymer composites (SMPCs) is proposed and applied to four-dimensional (4D) printed SMPCs. The multi-branch constitutive model is used to simulate the time- and temperature-dependent mechanical behavior of the shape memory polymer matrix. According to the elastic-viscoelastic correspondence principle, the equivalent viscoelastic stiffness tensor of the composite is obtained in the micromechanics framework of energy-based effective strain theory and the Mori-Tanaka homogenization scheme, in which a two-parameter interfacial damage model is adopted to consider the displacement discontinuity and traction continuity conditions at the interface between the inclusion and the matrix. The numerical integration scheme for the three-dimensional (3D) viscoelastic constitutive model of SMPCs is presented, and the finite element application is implemented by the user material subroutine UMAT of ABAQUS. After identifying the model parameters with experimental data, the tensile stress-strain curves and stress relaxation phenomena of 4D printed unidirectional SMPCs are successfully described by theoretical simulations. Besides, theoretical simulations also adequately predict the shape memory behavior of 4D printed composites and complex members.

1. Introduction

Thermotropic shape memory polymers (SMPs) are a kind of active materials that can sense external temperature changes and produce an autonomous deformation response, which are characterized by large deformability, variable stiffness and shape memory effects (Biswas et al., 2021; Elliott et al., 2020; King et al., 2021; Zeng et al., 2021). To facilitate the application of SMPs in practical engineering, systematic theoretical frameworks have been established to predict the thermo-mechanical behavior and shape memory effects of SMPs (Yu et al., 2012, 2014a; Fang et al., 2018; Gu et al., 2017, 2020; Liu et al., 2006; Nguyen et al., 2008; Qi et al., 2008; Zhao et al., 2020). For example, Liu et al. (2006) firstly developed a constitutive model of SMPs inspired by phase evolution theory, which assumes that SMP is composed of “active phase” and “frozen phase” and introduces internal variables such as storage

strain. Nguyen et al. (2008) proposed a thermo-viscoelastic model combining structural relaxation and stress relaxation based on viscoelastic theory, which can describe the dependence of SMPs on both strain rate and temperature change rate. Yu et al. (2012) innovatively proposed a multi-branch model similar to the generalized Maxwell model to quantitatively analyze the multiple shape memory effects of SMPs and the underlying physical mechanisms for the associated energy storage and release, providing a novel paradigm for theoretical modeling of SMPs. Gu et al. (2017) developed a thermodynamic constitutive model incorporating structural and stress relaxation based on an internal state variable modeling approach, which is highly valuable and provides new insights into the development of finite deformation theory for SMPs.

Shape memory polymer composites (SMPCs) blend SMPs and other reinforcing phases such as carbon nanotubes, metal micro-

* Corresponding author.

** Corresponding author.

E-mail addresses: lengjs@hit.edu.cn (J. Leng), yj_liu@hit.edu.cn (Y. Liu).

<https://doi.org/10.1016/j.mechmat.2022.104301>

Received 13 August 2021; Received in revised form 27 March 2022; Accepted 27 March 2022

Available online 5 April 2022

0167-6636/© 2022 Elsevier Ltd. All rights reserved.

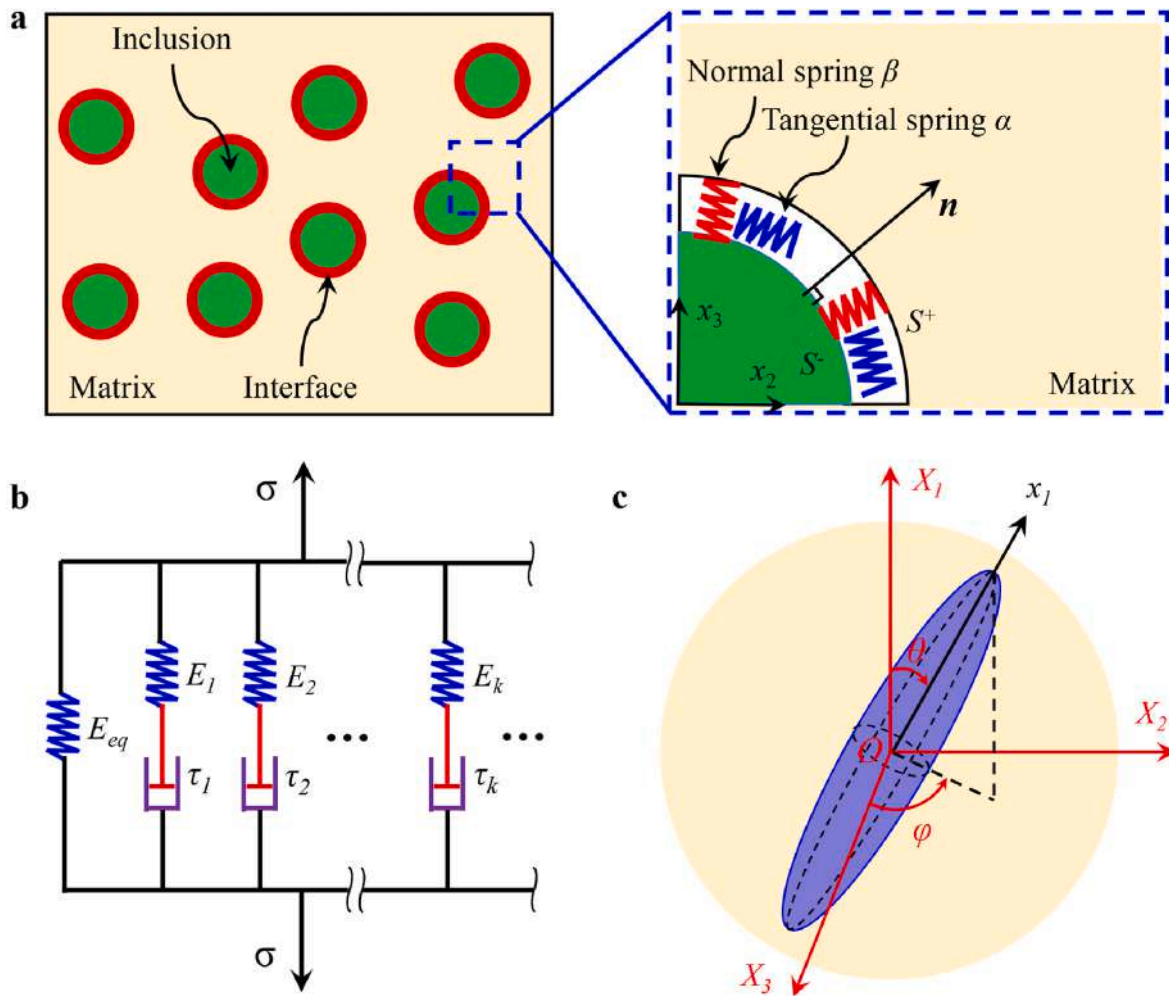


Fig. 1. A micromechanical equivalent model for the inclusion problem with imperfect interface. a) Schematic of the interface spring model. b) Multi-branch viscoelastic model of SMP matrix. c) The global coordinate system ($O-X_1X_2X_3$) and the local coordinate system ($O-x_1x_2x_3$) for an elliptical inclusion.

nanoparticles, chopped fibers or long fibers to improve the mechanical properties of SMPs. Moreover, the emerging four-dimension (4D) printing technology provides a convenient, short-cycle and low-cost solution for the manufacturing and structural customization of SMPCs (Zeng et al., 2022). As a result, SMPCs possess the potential to serve as structural and functional materials for engineering applications such as space deployable structures, bio-devices, smart robotics and flexible electronics due to their excellent mechanical properties, rapid customizability and exceptional shape memory effects (Xia et al., 2021). However, the anisotropy of composites has prompted researchers to seek new modeling approaches to describe the anisotropic thermodynamic behavior of SMPCs (Ge et al., 2016; Gu et al., 2019; Mao et al., 2015; Tan et al., 2014). Combining the composite bridge model and the phase evolution theory of SMPs, Tan et al. (2014) developed a constitutive model of SMPCs under small deformation. Ge et al. (2016) constructed a thermodynamic constitutive framework based on the phase evolution principle to describe the large deformation thermodynamic behavior of three-dimension (3D) printed anisotropic composites, but the constitutive framework did not consider the effect of loading rate. Gu et al. (2019) established a thermo-viscoelastic model for unidirectional SMPCs using an internal state variable modeling approach, which can be applied in a finite deformation range.

In the constitutive models of SMPCs presented above, the contributions of the reinforcing phases to the thermodynamic properties of SMPCs are considered simply by the volume averaging method, failing to model the interactions and interfacial effects between the matrix and

the reinforcing phases. In view of this, several equivalent constitutive models of SMPCs based on micromechanics have been preliminarily proposed (Hassanzadeh-Aghdam et al., 2019; Jarali et al., 2018; Su et al., 2020; Zhao et al., 2019). Jarali et al. (2018) extended Eshelby's equivalent inclusion theory to multiphase SMPCs, and combined the simple one-dimensional phase transition model of SMPs to obtain the constitutive model of SMPCs under small deformation. Zhao et al. (2019) combined the generalized Maxwell model of SMPs with the Mori-Tanaka scheme to establish a micromechanical model for multi-walled carbon nanotube-reinforced SMPCs. To further develop the model, Xin et al. (2021) proposed a gradient interface model to consider the interfacial effects between the reinforcing phases and the SMP matrix. Despite these advances, a systematic micromechanical framework for SMPCs is still lacking here, which incorporates the thermal viscoelasticity of SMPs, the imperfection of the interface and the multiphase reinforcement effect. Moreover, finite element implementation of micromechanical constitutive models for SMPCs is rarely reported.

In this study, a micromechanical thermo-viscoelastic constitutive model of multiphase SMPCs based on energy-based effective strain theory and the Mori-Tanaka homogenization scheme is proposed and applied in 4D printed composites, where the thermodynamic properties of the SMP matrix are described by a multi-branch model. The outline of the paper is as follows. In Section 2, details of the micromechanical modeling of SMPCs are presented, where interfacial imperfection and thermal viscoelasticity of the matrix are taken into account. In Section 3, the numerical integration scheme for the proposed 3D model is

developed and finite element simulations are implemented by the user material subroutine UMAT of ABAQUS. In Section 4, 4D printed composites are fabricated and corresponding experiments are performed to characterize their thermodynamic properties. In Section 5, thermodynamic experimental data are applied for parameter identification and model validation. In Section 6, some conclusions are given.

2. Micromechanical modeling

A viscoelastic constitutive model based on micromechanics is derived for SMPCs composed of SMP matrix and elliptical inclusions. Firstly, assuming that both the matrix and inclusions are elastic materials, the interfacial imperfection is considered based on the modified Eshelby's inclusion principle. Secondly, the energy-based effective strain theory and Mori-Tanaka method are combined to obtain the equivalent elastic stiffness tensor of unidirectional composites. Finally, considering the thermo-viscoelastic characteristics of the matrix under the small strain assumption, the macro-viscoelastic properties of the composites are obtained according to the elastic-viscoelastic correspondence principle.

2.1. Modified Eshelby inclusion problem

For multiphase composites composed of the matrix and multiple inclusions, we assume that the interface between each type of inclusion and the matrix is imperfect. As shown in Fig. 1a, the imperfect interface is simulated as a linear spring layer with no thickness, which has continuous traction but discontinuous displacement field, and the discontinuity conditions can be expressed as (Bennett et al., 2018)

$$\llbracket \boldsymbol{\sigma} \rrbracket \cdot \mathbf{n} = [\boldsymbol{\sigma}(S^+) - \boldsymbol{\sigma}(S^-)] \cdot \mathbf{n} = 0 \quad (1a)$$

$$\llbracket \mathbf{u} \rrbracket = \mathbf{u}(S^+) - \mathbf{u}(S^-) = \boldsymbol{\eta} \cdot \boldsymbol{\sigma} \cdot \mathbf{n} \quad (1b)$$

where S and \mathbf{n} denote the interface and its outward unit normal vector, and the superscripts $+$ and $-$ denote the positive and negative sides, respectively. $\llbracket \boldsymbol{\sigma} \rrbracket$ is the traction difference between the positive and negative sides of the interface, and $\llbracket \mathbf{u} \rrbracket$ is the interface displacement jump. $\boldsymbol{\eta}$ is a second-order tensor representing the compliance of the interface spring, assuming it is symmetric and positive definite. $\boldsymbol{\eta} \rightarrow 0$ indicates perfect bonding, while $\boldsymbol{\eta} \rightarrow \infty$ indicates complete debonding. Assume that the components of the interface compliance tensor follow the form:

$$\eta_{ij} = \alpha \delta_{ij} + (\beta - \alpha) n_i n_j \quad (2)$$

where α and β denote the tangential and normal compliance of the interface, respectively. Considering the inclusion with imperfect interface in the infinite domain, following the work of Qu (1993), the integral form of the perturbed strain field caused by the r -th type of inclusion is obtained as

$$\begin{aligned} \bar{\boldsymbol{\varepsilon}}_r^*(\mathbf{x}) = & \int_{V_r} \boldsymbol{\Gamma}^\infty(\mathbf{x} - \mathbf{x}') : \mathbb{C}_0 : \boldsymbol{\varepsilon}_r^{**}(\mathbf{x}') dv_r' + \int_{S'} \boldsymbol{\Gamma}^\infty(\mathbf{x} - \mathbf{x}') : \mathbb{C}_0 : \llbracket \mathbf{u}_r(\mathbf{x}') \rrbracket \otimes \mathbf{n} ds' \\ & - \int_{S'} \nabla_x^s \nabla_x^s \mathbf{g}^\infty(\mathbf{x} - \mathbf{x}') \cdot \llbracket \boldsymbol{\sigma}(\mathbf{x}') \rrbracket \cdot \mathbf{n} ds' \end{aligned} \quad (3)$$

where $\bar{\boldsymbol{\varepsilon}}_r^*$ is the perturbed strain in the inclusion relative to the medium, and $\boldsymbol{\varepsilon}_r^{**}$ is the eigenstrain in the inclusion. \mathbb{C}_0 is the elastic stiffness tensor of the homogeneous medium. V is the volume domain of the inclusion, which contains the imperfect interface S . $\boldsymbol{\Gamma}^\infty(\mathbf{x} - \mathbf{x}')$ is a fourth-order tensor associated with the medium and is defined as follows (Bennett et al., 2018)

$$\boldsymbol{\Gamma}^\infty(\mathbf{x} - \mathbf{x}') = \nabla_x^s \nabla_x^s \mathbf{g}^\infty(\mathbf{x} - \mathbf{x}') \quad (4)$$

where $\mathbf{g}^\infty(\mathbf{x} - \mathbf{x}')$ is the second-order Green's function. The detailed

derivation of Eq. (3) is presented in Supplementary material S1.

Now assuming that the eigenstrain in the inclusion is uniformly distributed and applying Eq. (1a), the perturbed strain $\bar{\boldsymbol{\varepsilon}}_r^*$ averaged over the inclusion volume V_r is given by:

$$\begin{aligned} \bar{\boldsymbol{\varepsilon}}_r^* = & \frac{1}{V_r} \int_{V_r} \int_{V_r'} \boldsymbol{\Gamma}^\infty(\mathbf{x} - \mathbf{x}') : \mathbb{C}_0 : \boldsymbol{\varepsilon}_r^{**} dv_r' dv_r \\ & + \frac{1}{V_r} \int_{V_r} \int_{S'} \boldsymbol{\Gamma}^\infty(\mathbf{x} - \mathbf{x}') : \mathbb{C}_0 : \llbracket \mathbf{u}_r(\mathbf{x}') \rrbracket \otimes \mathbf{n} ds' dv_r \end{aligned} \quad (5)$$

The fourth-order interior polarization tensor \mathbb{P}_r is introduced

$$\mathbb{P}_r = \int_{V_r} \boldsymbol{\Gamma}^\infty(\mathbf{x} - \mathbf{x}') dv_r \quad \text{for } \mathbf{x}' \in V_r \quad (6)$$

Permute the integration order of the first integral term in Eq. (5) to obtain

$$\bar{\boldsymbol{\varepsilon}}_r^* = \mathbb{S}_r : \boldsymbol{\varepsilon}_r^{**} + \frac{1}{V_r} \int_{V_r} \int_{S'} \boldsymbol{\Gamma}^\infty(\mathbf{x} - \mathbf{x}') : \mathbb{C}_0 : \llbracket \mathbf{u}_r(\mathbf{x}') \rrbracket \otimes \mathbf{n} ds' dv_r \quad (7)$$

where $\mathbb{S}_r = \mathbb{P}_r : \mathbb{C}_0$, \mathbb{S}_r is fourth-order interior-point Eshelby tensor.

In the framework of the spring interface model described by Eq. (1), the second integral term in Eq. (7) can be simplified by a series of conversions according to the method proposed by Dinzart and Sabar (2017):

$$\frac{1}{V_r} \int_{V_r} \int_{S'} \boldsymbol{\Gamma}^\infty(\mathbf{x} - \mathbf{x}') : \mathbb{C}_0 : \llbracket \mathbf{u}_r(\mathbf{x}') \rrbracket \otimes \mathbf{n} ds' dv_r = (\mathbb{S}_r - \mathbb{I}) : \mathbb{R}_r : \mathbb{C}_r : \bar{\boldsymbol{\varepsilon}}_r \quad (8)$$

where $\bar{\boldsymbol{\varepsilon}}_r$ is the strain averaged over the inclusion volume V_r . \mathbb{I} is the fourth-order identity tensor. \mathbb{C}_r is the elastic stiffness tensor of the r -th type of inclusion. The fourth-order tensor \mathbb{R}_r describes the comprehensive influence of the interface parameters and the configuration of the inclusion, which is defined as (Dinzart and Sabar, 2017)

$$\mathbb{R}_{r,ijmn}^r = \frac{1}{4V_r} \int_S (\eta_{im} \eta_j \eta_n + \eta_{jm} \eta_i \eta_n + \eta_{in} \eta_j \eta_m + \eta_{jn} \eta_i \eta_m) \quad (9)$$

Applying Eq. (8) in Eq. (7) gives

$$\bar{\boldsymbol{\varepsilon}}_r^* = \mathbb{S}_r : \boldsymbol{\varepsilon}_r^{**} + (\mathbb{S}_r - \mathbb{I}) : \mathbb{R}_r : \mathbb{C}_r : \bar{\boldsymbol{\varepsilon}}_r \quad (10)$$

2.2. Micromechanics framework

The strain energy in the composite is determined by the sum of the strain energy of the matrix and the multiphase inclusions (Saadat et al., 2015)

$$\int_V \boldsymbol{\sigma}_{eq}^T : \boldsymbol{\varepsilon}_{eq} dv = \int_{V_0} \boldsymbol{\sigma}_0^T : \boldsymbol{\varepsilon}_0 dV_0 + \sum_{r=1}^N \int_{V_r} \boldsymbol{\sigma}_r^T : \boldsymbol{\varepsilon}_r dv_r \quad (11)$$

where $\boldsymbol{\sigma}_{eq}$ and $\boldsymbol{\varepsilon}_{eq}$ are the equivalent stress tensor and equivalent strain tensor in the composite, respectively. $\boldsymbol{\sigma}_0$ and $\boldsymbol{\varepsilon}_0$ are the stress tensor and strain tensor in the matrix, respectively. $\boldsymbol{\sigma}_r$ and $\boldsymbol{\varepsilon}_r$ are respectively the stress tensor and strain tensor in the r -th type of inclusion. V , V_0 and V_r are the total volume of the composite, the volume of the matrix, and the volume of the r -th type of inclusion, respectively.

Herein, we define the effective stress $\langle \boldsymbol{\sigma}_k \rangle = \langle \boldsymbol{\sigma}_{ij}^k \rangle \mathbf{e}_i \otimes \mathbf{e}_j$ and effective strain $\langle \boldsymbol{\varepsilon}_k \rangle = \langle \boldsymbol{\varepsilon}_{ij}^k \rangle \mathbf{e}_i \otimes \mathbf{e}_j$ ($k = eq, 0, 1, \dots, N$) for the composite and all constituent phases so that the following equation holds

$$\int_{V_k} \boldsymbol{\sigma}_k^T : \boldsymbol{\varepsilon}_k dv_k = \int_{V_k} (\mathbb{C}_k : \boldsymbol{\varepsilon}_k)^T : \boldsymbol{\varepsilon}_k dv_k = (\mathbb{C}_k : \langle \boldsymbol{\varepsilon}_k \rangle) : \langle \boldsymbol{\varepsilon}_k^T \rangle V_k \quad (12)$$

Subsequently, Eq. (11) can be expressed as

$$(\mathbb{C}_{eq} : \langle \boldsymbol{\varepsilon}_{eq} \rangle) : \langle \boldsymbol{\varepsilon}_{eq}^T \rangle V = (\mathbb{C}_0 : \langle \boldsymbol{\varepsilon}_0 \rangle) : \langle \boldsymbol{\varepsilon}_0^T \rangle V_0 + \sum_{r=1}^N (\mathbb{C}_r : \langle \boldsymbol{\varepsilon}_r \rangle) : \langle \boldsymbol{\varepsilon}_r^T \rangle V_r \quad (13)$$

The effective stress of the composite is

$$\langle \boldsymbol{\sigma}_{eq} \rangle = \xi_0 \langle \boldsymbol{\sigma}_0 \rangle + \sum_{r=1}^N \xi_r \langle \boldsymbol{\sigma}_r \rangle \quad (14)$$

where $\xi_0 = \frac{V_0}{V}$ and $\xi_r = \frac{V_r}{V}$ are the volume fractions of the homogeneous matrix and the r -th type of inclusion, respectively, and $\xi_0 + \sum_{r=1}^N \xi_r = 1$.

The Mori-Tanaka scheme is extended to express the effective strain tensors of the matrix and each inclusion as (Liu and Bian, 2019)

$$\langle \boldsymbol{\varepsilon}_0 \rangle = \langle \boldsymbol{\varepsilon}_{eq} \rangle + \sum_{j=1}^N \langle \tilde{\boldsymbol{\varepsilon}}_j \rangle \quad (15a)$$

$$\langle \boldsymbol{\varepsilon}_r \rangle = \langle \boldsymbol{\varepsilon}_{eq} \rangle + \sum_{j=1}^N \langle \tilde{\boldsymbol{\varepsilon}}_j \rangle + \langle \boldsymbol{\varepsilon}_r^* \rangle \quad (15b)$$

where $\langle \tilde{\boldsymbol{\varepsilon}}_j \rangle$ is the effective perturbed strain tensor superimposed on the equivalent strain due to the existence of the corresponding inclusion. $\langle \boldsymbol{\varepsilon}_r^* \rangle$ is the effective perturbed strain tensor in each inclusion relative to the matrix.

According to Eshelby's equivalence principle, here is (Zhang et al., 2020)

$$\mathbb{C}_r : \langle \boldsymbol{\varepsilon}_r \rangle = \mathbb{C}_0 : (\langle \boldsymbol{\varepsilon}_r \rangle - \boldsymbol{\varepsilon}_r^{**}) \quad (16)$$

Then the volume average strain is replaced by the effective strain in Eq. (10).

$$\langle \boldsymbol{\varepsilon}_r^* \rangle = \mathbb{S}_r : \boldsymbol{\varepsilon}_r^{**} + (\mathbb{S}_r - \mathbb{I}) : \mathbb{R}_r : \mathbb{C}_r : \langle \boldsymbol{\varepsilon}_r \rangle \quad (17)$$

Using Eq. (15) and Eq. (16) in Eq. (17) then gives

$$\langle \boldsymbol{\varepsilon}_r \rangle = [\mathbb{I} + \mathbb{S}_r : \mathbb{C}_0^{-1} : (\mathbb{C}_r - \mathbb{C}_0) + (\mathbb{I} - \mathbb{S}_r) : \mathbb{R}_r : \mathbb{C}_r]^{-1} : \langle \boldsymbol{\varepsilon}_0 \rangle \quad (18)$$

The fourth-order strain concentration tensor \mathbb{A}_r is defined: $\mathbb{A}_r = [\mathbb{I} + \mathbb{S}_r : \mathbb{C}_0^{-1} : (\mathbb{C}_r - \mathbb{C}_0) + (\mathbb{I} - \mathbb{S}_r) : \mathbb{R}_r : \mathbb{C}_r]^{-1}$. Note that $\langle \boldsymbol{\sigma}_{eq} \rangle = \mathbb{C}_{eq} : \langle \boldsymbol{\varepsilon}_{eq} \rangle$, the effective strain tensors in each phase are obtained by combining Eqs. (14) and (18)

$$\langle \boldsymbol{\varepsilon}_r \rangle = \mathbb{T}_r : \mathbb{C}_{eq} : \langle \boldsymbol{\varepsilon}_{eq} \rangle \quad (19)$$

where \mathbb{T}_r is the fourth-order transformation tensor, which is expressed as: $\mathbb{T}_r = \mathbb{A}_r : (\xi_0 \mathbb{C}_0 : \mathbb{A}_0 + \sum_{j=1}^N \xi_j \mathbb{C}_j : \mathbb{A}_j)^{-1}$, where $\mathbb{A}_0 = \mathbb{I}$. Substituting Eq. (19) into Eq. (13) gives

$$\mathbb{C}_{eq} = \xi_0 (\mathbb{T}_0 : \mathbb{C}_{eq})^T : \mathbb{C}_0 : (\mathbb{T}_0 : \mathbb{C}_{eq}) + \sum_{r=1}^N \xi_r (\mathbb{T}_r : \mathbb{C}_{eq})^T : \mathbb{C}_r : (\mathbb{T}_r : \mathbb{C}_{eq}) \quad (20)$$

Since both \mathbb{C}_r and \mathbb{A}_r are symmetric tensors, the equivalent stiffness of the multiphase composite can be obtained from Eq. (20)

$$\mathbb{C}_{eq} = \left[\xi_0 \mathbb{T}_0 : \mathbb{C}_0 : \mathbb{T}_0 + \sum_{r=1}^N \xi_r \mathbb{T}_r : \mathbb{C}_r : \mathbb{T}_r \right]^{-1} \quad (21)$$

2.3. Effective viscoelastic stiffness

The constitutive relationship for isotropic linear viscoelastic matrix in the time domain is given as (Barbero, 2013)

$$\boldsymbol{\sigma}(t) = \int_0^t \lambda(t-\tau) \mathbf{I} \otimes \mathbf{I} : \dot{\boldsymbol{\varepsilon}}(\tau) d\tau + \int_0^t 2\mu(t-\tau) \mathbb{I} : \dot{\boldsymbol{\varepsilon}}(\tau) d\tau \quad (22)$$

where $\boldsymbol{\sigma}(t)$ and $\boldsymbol{\varepsilon}(t)$ are the stress tensor and strain tensor, respectively, and the point above the strain tensor represents the differentiation with respect to time. \mathbf{I} and \mathbb{I} are the second- and fourth-order identity tensors. $\lambda(t)$ and $\mu(t)$ are the viscoelastic Lamé constants, which are denoted as

$$\lambda(t) = \frac{v(t)E(t)}{[1+v(t)][1-2v(t)]}, \quad \mu(t) = \frac{E(t)}{2[1+v(t)]} \quad (23a,b)$$

where $E(t)$ denotes the stress relaxation modulus and $v(t)$ denotes the Poisson's ratio.

To develop a small strain constitutive model, the rheological model composed of a hyperelastic spring and multiple parallel Maxwell elements shown in Fig. 1b is applied to model the viscoelastic behavior of the SMP matrix, whose stress relaxation modulus in the time domain is given by (Yu et al., 2014b)

$$E(t) = E_\infty + \sum_{k=1}^N E_k \exp\left(-\frac{t}{\tau_k}\right) \quad (24)$$

where E_∞ is the equilibrium modulus, E_k is the relaxation modulus, and τ_k is the relaxation time.

The Laplace transform of a function $f(t)$ in the time domain (t -domain) maps to the Laplace domain (s -domain) as $\hat{f}(s)$. The Laplace transform is defined as $L[f(t)] = \hat{f}(s) = \int_0^\infty f(t)e^{-st} dt$, where s is a complex variable in the Laplace domain. Subsequently, Eq. (22) can be expressed in the Laplace domain as

$$\hat{\boldsymbol{\sigma}}(s) = s\hat{\lambda}(s)\mathbf{I} \otimes \mathbf{I} : \hat{\boldsymbol{\varepsilon}}(s) + 2s\hat{\mu}(s)\mathbb{I} : \hat{\boldsymbol{\varepsilon}}(s) = s\hat{\mathbb{C}}_0(s) : \hat{\boldsymbol{\varepsilon}}(s) \quad (25)$$

For simplicity, the Poisson's ratio of the matrix is assumed to remain constant here, i.e., $v(t) = v$.

Considering the elastic-viscoelastic correspondence principle, based on Eq. (21), the equivalent stiffness of a multiphase composite in the Laplacian domain is expressed as

$$s\hat{\mathbb{C}}_{eq}(s) = s \left[\xi_0 \hat{\mathbb{T}}_0(s) : \hat{\mathbb{C}}_0(s) : \hat{\mathbb{T}}_0(s) + \sum_{r=1}^N \xi_r \hat{\mathbb{T}}_r(s) : \hat{\mathbb{C}}_r(s) : \hat{\mathbb{T}}_r(s) \right]^{-1} \quad (26)$$

The effective stiffness of the viscoelastic composite in the time domain is subsequently obtained by the inverse Laplace transform:

$$\mathbb{C}_{eq}(t) = L^{-1}[\hat{\mathbb{C}}_{eq}(s)] \quad (27)$$

For the composite with the inclusion direction aligned with the overall coordinate system, the analysis is performed in the local coordinate system $O-x_1x_2x_3$, whose axis x_1 coincides with the rotation axis of the inclusion. However, the influence of the inclusion orientation on the equivalent properties of the composite should be considered in practice. In the spherical coordinate system $O-X_1X_2X_3$ as shown in Fig. 1c, the spatial distribution of the inclusion is described by two Euler angles θ and φ . The equivalent viscoelastic stiffness tensor of the composite in the global coordinate system is expressed as

$$\vec{\mathbb{C}}_{eq}(t) = \mathbb{L} : \mathbb{C}_{eq}(t) : \mathbb{L}^{-1} \quad (28)$$

where \mathbb{L} is the coordinate transformation tensor.

Since the SMP matrix is considered as a thermo-rheologically simple material, its viscoelastic behavior follows the time-temperature superposition principle (TTSP). The relaxation time of the k -th nonequilibrium branch at temperature T is denoted as

$$\tau_k = \alpha_T(T) \tau_k^0 \quad (29)$$

where $\alpha_T(T)$ is the TTSP shift factor and τ_k^0 is the relaxation time of the k -th nonequilibrium branch at the reference temperature. At temperatures around or above T_s , the TTSP shift factor $\alpha_T(T)$ is calculated by the Williams-Landel-Ferry (WLF) equation (Mao et al., 2019)

$$\log \alpha_T(T) = -\frac{C_1(T - T_r)}{C_2 + (T - T_r)} \quad (30)$$

where C_1 and C_2 are material constants. When the temperature is below T_s , $\alpha_T(T)$ follows Arrhenius type behavior (Mao et al., 2019)

$$\ln \alpha_T(T) = -\frac{AF_c}{k_b} \left(\frac{1}{T} - \frac{1}{T_g} \right) \quad (31)$$

Table 1
Material parameters for the carbon fiber (Liu et al., 2013).

Longitudinal modulus E_{f1} (GPa)	Transverse modulus E_{f2} (GPa)	Shear modulus G_{f12} (GPa)	Poisson's ratio, ν_{f12}	Poisson's ratio, ν_{f23}	Longitudinal CTE, μ_{f1} (K^{-1})	Transverse CTE, μ_{f2} (K^{-1})
220.69	13.79	8.97	0.2	0.25	-4.1×10^{-7}	5.6×10^{-6}

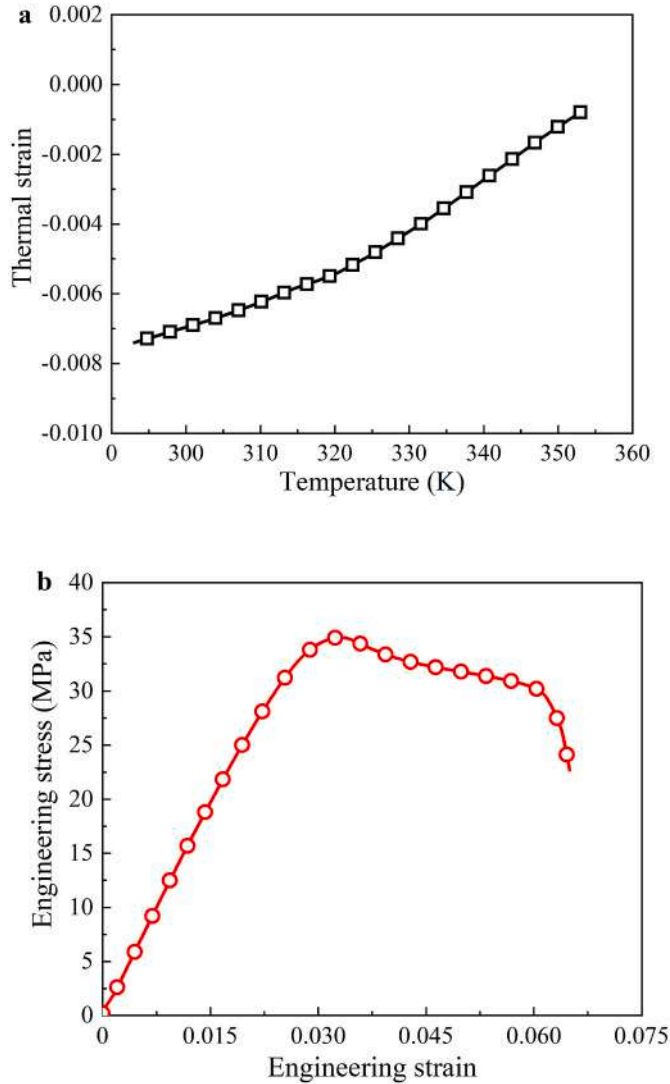


Fig. 2. a) CTE curve and b) uniaxial tensile curve at 293 K of SMP matrix.

where A and F_c are material constants, k_b is Boltzmann's constant. Here, T_s is calculated by equating $\alpha_T(T)$ in Eqs. (30) and (31). It is worth noting that the unit of temperature T and T_r in Eq. (30) is $^{\circ}C$, while the unit of temperature T and T_g in Eq. (31) is the thermodynamic temperature unit K.

3. Finite element implementation

To implement the finite element analysis of the viscoelastic relaxation phenomenon and shape memory behavior of SMPs, the user

material subroutine UMAT of ABAQUS was written in Fortran language, which followed the numerical integration scheme presented below.

In the Voigt notation, the equivalence between the components C_{ijkl} of the fourth-order tensor C and the components C_{IJ} of the 6×6 matrix C is $C_{ijkl} = C_{IJ}$. Thus, the equivalent viscoelastic stiffness tensor $C_{eq}(t)$ of the composite obtained from Eq. (27) can be expressed as a 6×6 stiffness matrix, whose components have the following form

$$C_{IJ}^{eq}(t) = C_{IJ,\infty}^{eq} + \sum_{k=1}^N C_{IJ,k}^{eq} \exp\left(-\frac{t}{\alpha_T \tau_k^0}\right) \quad (32)$$

where $C_{IJ,\infty}^{eq}$ and $C_{IJ,k}^{eq}$ are the equilibrium stiffness coefficient and the k -th relaxation stiffness coefficient, respectively.

For the linear viscoelastic composite, the stress-strain relationship at any time t is given by the Boltzmann superposition integral (Zobeiry et al., 2016)

$$\sigma_I(t) = \int_0^t C_{IJ}^{eq}(t-\tau) \frac{d\varepsilon_J}{d\tau} d\tau \quad (33)$$

where σ_I and ε_J are the components of the stress tensor and strain tensor when the Voigt notation is used, respectively.

The current state of the viscoelastic composite depends not only on the current value of the relaxation stiffness matrix but also on the loading history. Therefore, Eq. (33) must be evaluated at each increment of the finite element analysis. The method proposed by (Zocher et al., 1997; Gomez-Delrio and Kwok, 2020) is applied to acquire the incremental form of Eq. (33) as follows

$$\sigma_I(t_{n+1}) = \sigma_I(t_n) + \Delta\sigma_I(t_{n+1}) \quad (34)$$

where $\sigma_I(t_{n+1})$ is the stress of a specific element at the current time increment. t_{n+1} and t_n are the current time and the time before the increment occurs, respectively. $\Delta\sigma_I(t_{n+1})$ denotes the incremental change in stress of each element over the current time step, which is calculated as follows

$$\Delta\sigma_I(t_{n+1}) = C_{IJ}^*(t_{n+1})[\Delta\varepsilon_J(t_{n+1}) - \mu_J \Delta T(t_{n+1})] - \Delta\sigma_I^R(t_n) \quad (35)$$

where μ_J is the coefficient of thermal expansion (CTE) and ΔT is the temperature increment. $\Delta\varepsilon_J(t_{n+1})$ is the change in strain between the previous and current increment, which is assumed to vary linearly with time. $C_{IJ}^*(t_{n+1})$ and $\Delta\sigma_I^R(t_n)$ can be written as (Gomez-Delrio and Kwok, 2020)

$$C_{IJ}^*(t_{n+1}) = C_{IJ,\infty}^{eq} + \frac{1}{\Delta t_{n+1}} \sum_{k=1}^N \alpha_T \tau_k^0 C_{IJ,k}^{eq} \left[1 - \exp\left(-\frac{\Delta t_{n+1}}{\alpha_T \tau_k^0}\right)\right] \quad (36)$$

$$\Delta\sigma_I^R(t_n) = \sum_{k=1}^N \left[1 - \exp\left(\frac{-\Delta t_n}{\alpha_T \tau_k^0}\right)\right] \sum_{j=1}^6 \Phi_{IJ,k}(t_n) \quad (37)$$

where Φ_{IJ} is a vector of length N that will be stored for use in the next increment, and whose components can be expressed as

$$\Phi_{IJ,k}(t_n) = \Phi_{IJ,k}(t_{n-1}) \exp\left(\frac{-\Delta t_n}{\alpha_T \tau_k^0}\right) + \alpha_T \tau_k^0 C_{IJ,k}^{eq} \left[\frac{\Delta\varepsilon_J(t_n) - \mu_J \Delta T(t_n)}{\Delta t_n} \right] \left[1 - \exp\left(\frac{-\Delta t_n}{\alpha_T \tau_k^0}\right)\right] \quad (38)$$

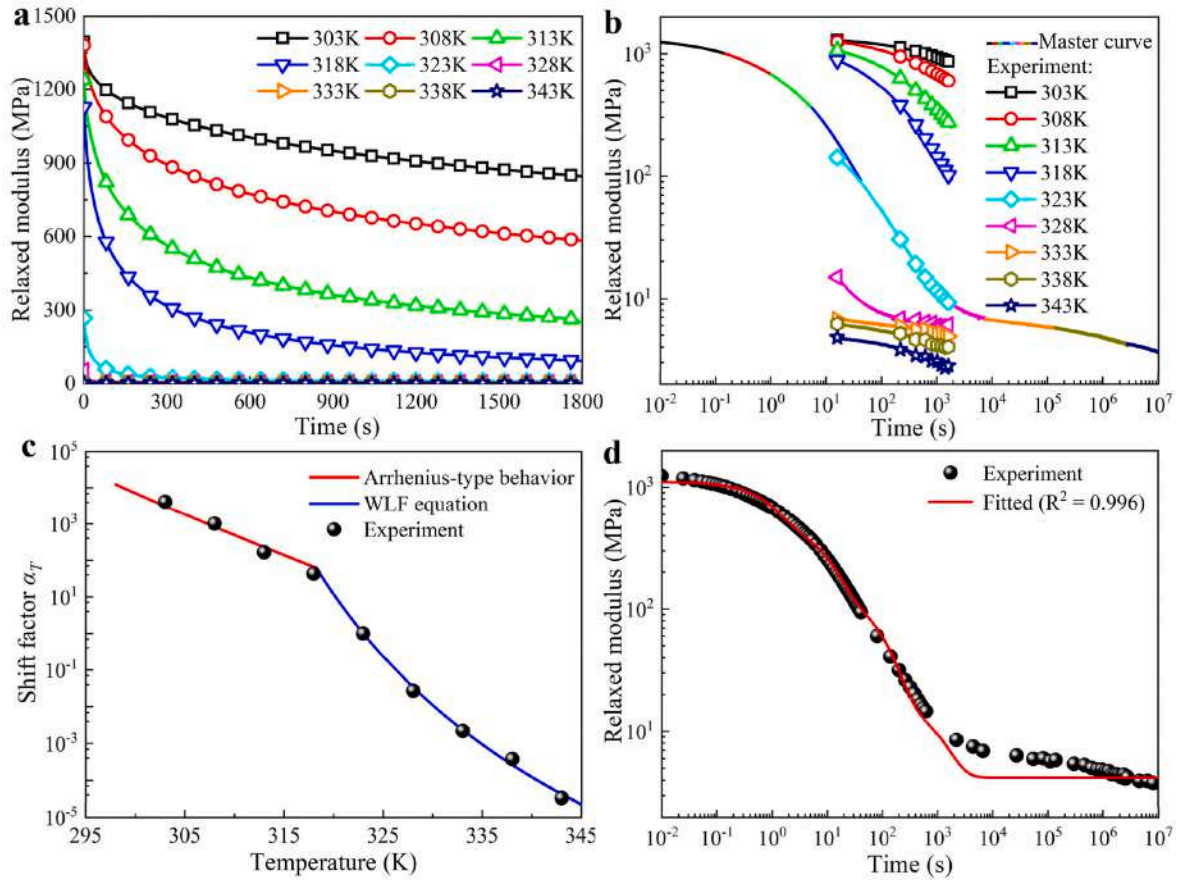


Fig. 3. Stress relaxation tests on SMP matrix. a) The stress relaxation curves of the SMP matrix from 303 K to 343 K with an interval of 5 K. b) The stress relaxation master curve at 323 K obtained by the TTSP. c) Experimental and theoretically fitted shift factors versus temperature. d) Theoretical fitting of the stress relaxation master curve.

The Jacobian matrix (or tangent stiffness) is a 6×6 matrix, which is defined as the derivative of the stress at the current time step with respect to the current strain, i.e. (Yapa Hamillage et al., 2022)

$$J = \frac{\partial \sigma_I(t_{n+1})}{\partial \epsilon_J(t_{n+1})} = C_{IJ,\infty}^{eq} + \frac{1}{\Delta t_{n+1}} \sum_{k=1}^N \alpha_T \tau_k^0 C_{IJ,k}^{eq} \left[1 - \exp\left(-\frac{\Delta t_{n+1}}{\alpha_T \tau_k^0}\right) \right] \quad (39)$$

4. Materials and experiments

4.1. Material and sample preparations

When the ratio of the semi-axial lengths of the x_1 axis to the x_2 axis, i.e., the aspect ratio, is infinitely large, elliptical inclusions with equal semi-axial lengths along the x_2 and x_3 axes tend to be cylindrical inclusions. Thus, long carbon fibers can be considered as elliptical inclusions with infinitely large aspect ratios. In this study, 4D printed unidirectional continuous fiber-reinforced SMPCs were used to verify the ability of the proposed micromechanical model to predict the stress relaxation and shape memory effect of SMPCs. The matrix material is a polylactic acid (PLA)-based SMP with a T_g of 336 K (Zhang et al., 2018). The inclusion phase is Toray T300-1000 carbon fiber, and its mechanical parameters are presented in Table 1. Unidirectional fiber-reinforced SMPC specimens with different fiber lay-up angles ($\theta = 0^\circ, 30^\circ, 45^\circ, 60^\circ$ and 90°) were fabricated by using a continuous fiber-reinforced composite 3D printer (Combot-200), and the fiber volume fraction of all specimens was 12%. The printing parameters for all specimens were set as: nozzle temperature of 493 K, printing speed of 100 mm/min, layer thickness of 0.3 mm, nozzle diameter of 1 mm and substrate

temperature of 333 K.

4.2. CTE measurements

Thermo-mechanical analysis (TMA) of PLA-based SMP was performed on a thermo-mechanical Analyzer (TMAQ400/Q400EM) to acquire the CTE of the matrix. Square SMP specimens with dimensions of $5.8 \times 5.8 \times 5.8$ mm were fabricated by 3D printing. A specimen was first heated from 298 K to 363 K at 2 K/min and held at 363 K for 10 min. The specimen was then cooled down to 273 K at 2 K/min and held at 273 K for 10 min. The specimen was finally reheated to 363 K at 2 K/min. Fig. 2a shows the CTE measurement during heating from 293 K to 353 K, from which the average CTE of the matrix can be obtained as $\mu_m = 0.0001/\text{K}$. The curve for cooling from 353 K to 293 K exhibits a similar result, which is not presented here for clarity.

4.3. Uniaxial tensile tests

The uniaxial tensile tests of PLA-based SMP and 4D printed unidirectional SMPCs were carried out using a Zwick/Roell universal testing machine with a temperature-controlled chamber. The tensile tests of SMP specimens were performed following the standard ASTM D638. The specimens are dumbbell-shaped with a dimension of $115 \times 6 \times 2$ mm. 4D printed SMPC specimens with $\theta = 0^\circ, 30^\circ, 45^\circ, 60^\circ$ and 90° were uniaxially stretched, where θ is the angle between the fiber direction and the loading direction. All specimens with a gauge length of 45 mm were stretched at 293 K with a strain rate of 0.001 s^{-1} . Fig. 2b presents the tensile stress-strain curve of the SMP specimen, from which the modulus of elasticity of the matrix can be obtained as $E_m = 1.3 \text{ GPa}$.

Table 2
The model parameters obtained from experimental measurements.

Parameter	T_f (K)	C_1	C_2 (°C)	$-AF_c/k_b$ (K)	T_f (K)	μ_1 (K ⁻¹)	μ_2 (K ⁻¹)
Value	323	12.9	39.0	24,829	318.2	3.7×10^{-6}	1.2×10^{-4}
Parameter	τ_1	τ_2	τ_3	τ_4	τ_5	τ_6	
Value	0.1	1	10	100	1000	10,000	
Parameter	E_1	E_2	E_3	E_4	E_5	E_6	E_0
Value (MPa)	224.8	455.7	432.5	97.1	15.1	3.8	3.9

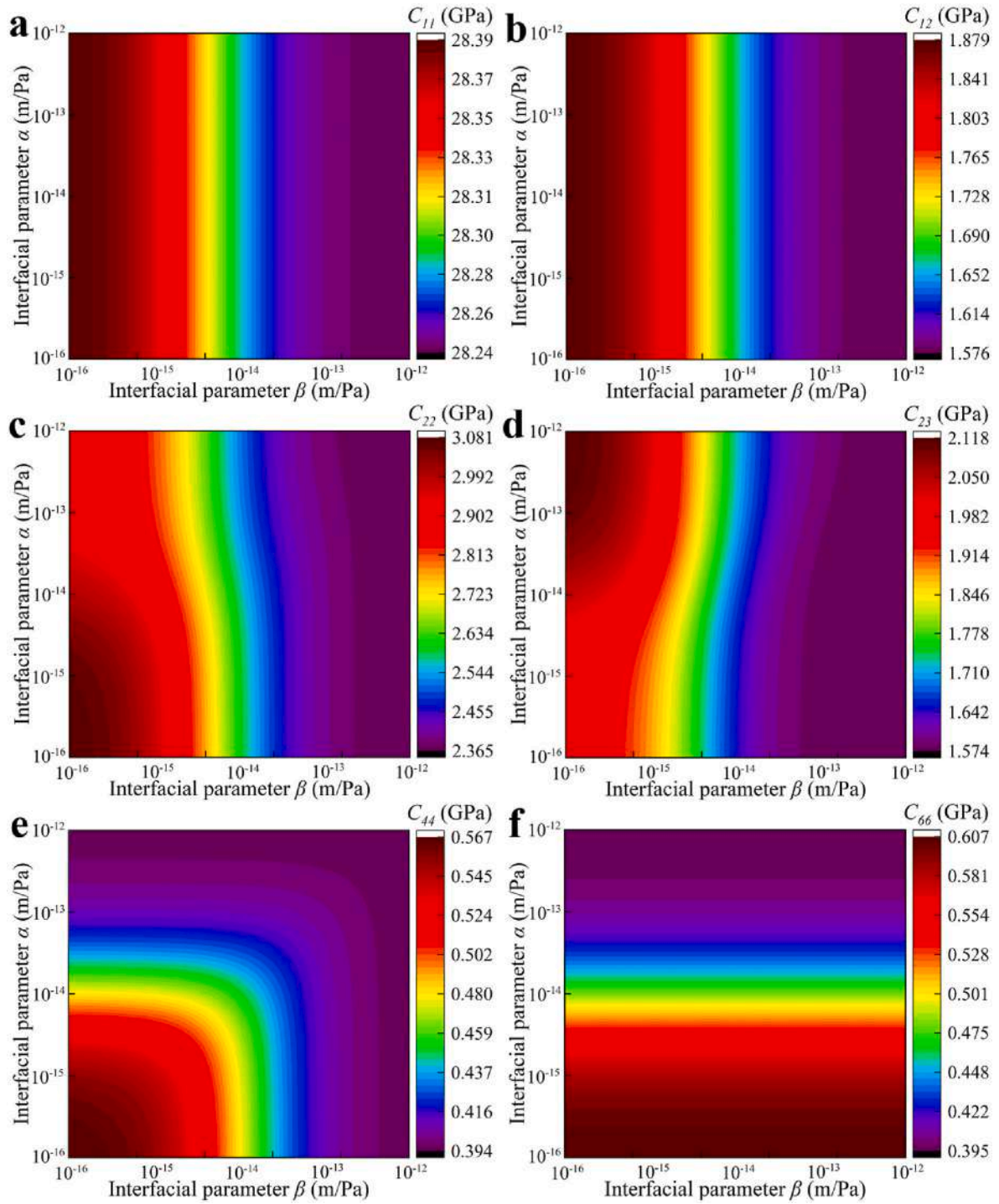


Fig. 4. The effect of two interfacial damage parameters on the equivalent stiffness coefficients of the composite for a fixed fiber volume fraction $\xi_f = 12\%$.

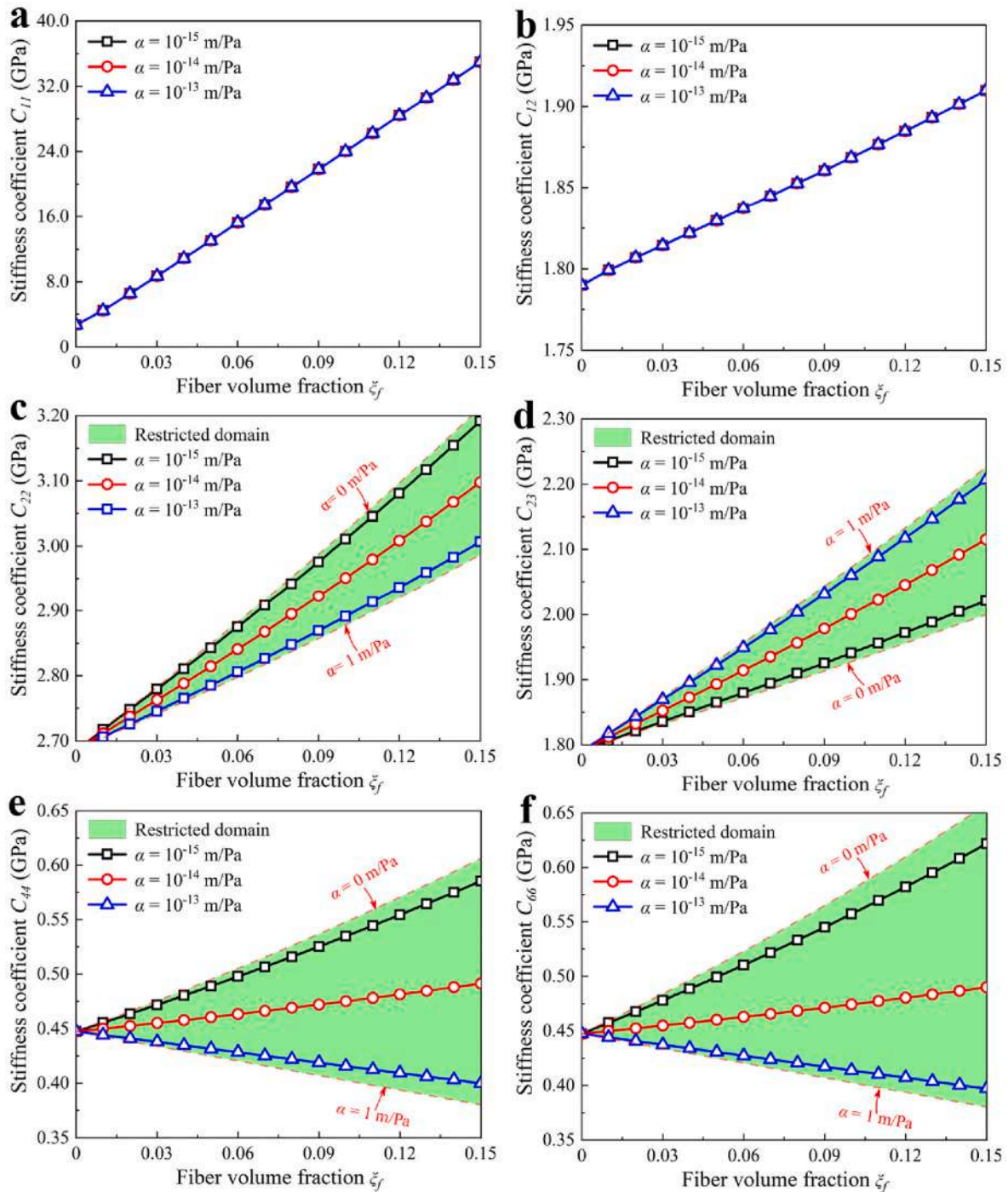


Fig. 5. Equivalent stiffness coefficients of the composite versus fiber volume fraction when varying the tangential interfacial parameter α .

Table 3

Viscoelastic stiffness coefficients of 4D printed unidirectional SMPs at a fiber volume fraction of $\xi_f = 12\%$.

K	∞	1	2	3	4	5	6
τ_k	–	0.1	1	10	100	1000	10,000
$C_{11,k}^{eq}$	26,489	377.2	697.5	655.2	146.3	22.7	5.7
$C_{12,k}^{eq}$	6.2	352.9	675.3	667.0	153.4	23.9	6.0
$C_{22,k}^{eq}$	10.2	573.8	1101.3	1093.9	252.6	39.4	9.9
$C_{23,k}^{eq}$	6.5	369.9	707.6	697.2	160.0	24.9	6.3
$C_{66,k}^{eq}$	2.0	106.0	205.8	209.4	49.3	7.7	1.9

4.4. Stress relaxation tests

To acquire viscoelastic parameters of the matrix, the isothermal tensile stress relaxation tests of PLA-based SMP specimens were conducted on the ZWICK-010 universal testing machine according to the standard ASTM D638. Tensile stress relaxation tests at various temperatures (293 K–343 K with an interval of 5 K) were performed. The relaxation tests were completed in three steps. First, the samples were kept at the test temperature for 15 min to achieve thermal equilibrium. Then the samples were stretched by 0.022 (Engineering strain) with a strain rate of 0.001 s^{-1} . Finally, the deformation was held for 30 min and the stress decay was recorded. Fig. 3a gives the evolution curves of the

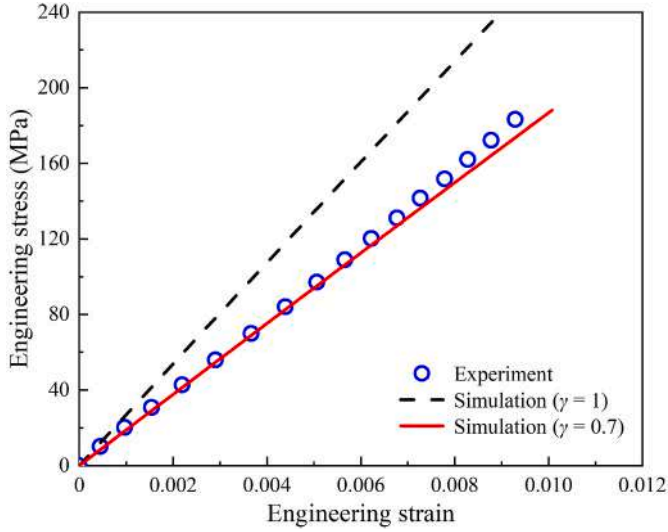


Fig. 6. Theoretical simulations and experimental measurements of uniaxial tensile curves of 4D printed SMPCs with fiber lay-up angle $\theta = 0^\circ$ at 293 K.

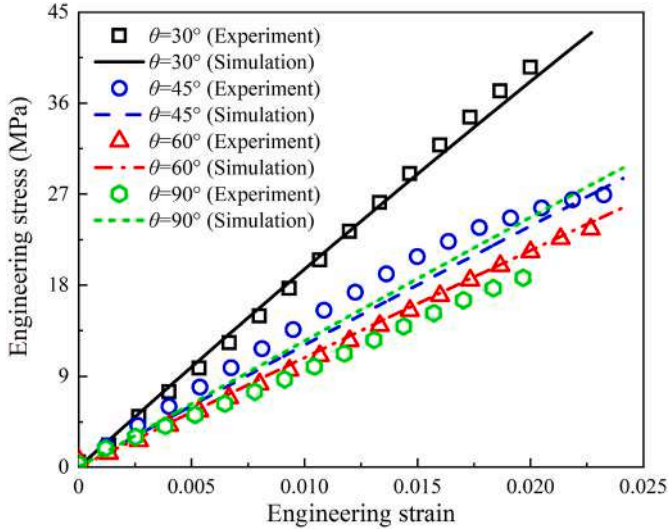


Fig. 7. Theoretical simulations and experimental measurements of uniaxial tensile results of 4D printed SMPCs at 293 K for different fiber lay-up angles θ .

relaxed modulus of the SMP matrix with time obtained from experiments at different temperatures. Similar to the relaxation test procedure for PLA-based SMP specimens, 4D printed SMPC specimens with $\theta = 30^\circ$, 45° , 60° and 90° were subjected to stress relaxation tests at 293 K and 323 K. The maximum loading strain was set to 0.011 restricted by the low elongation at break of the composite.

4.5. Shape memory cycle tests

Tensile shape memory cycle tests on 4D printed SMPC specimens with $\theta = 60^\circ$ were performed on the ZWICK-010 universal testing machine. The specimen size was $85 \times 20 \times 1.6$ mm and the loading gauge length was 45 mm. The shape memory cycle test was divided into five steps as follows. Step 1 (S1): The specimen was stretched to a prescribed strain (0.044) at 343 K. Step 2 (S2): The temperature was lowered to 299 K at a cooling rate of 2 K/min while maintaining the prescribed strain. Step 3 (S3): The load was removed while maintaining the temperature at 299 K. Step 4 (S4): The temperature was raised to 353 K at a heating rate of 4 K/min while keeping zero load. Step 5 (S5): The

temperature was kept at 353 K for 10 min. It should be pointed out that the actual cooling and heating rates were not constant due to the limitations of the temperature-controlled chamber used in the tests.

In addition, the free shape recovery test of a cross-shaped 4D printed SMPC member was carried out to demonstrate the ability of the developed model to predict the free shape recovery of complex composite structures. In this SMPC member, the fibers were laid at an angle of 45° . The experimental procedure is as follows. Firstly, the four free branches of the member were rotated at a certain angle to obtain an inwardly rolled temporary shape at a temperature of 343 K. Then the temperature was lowered to 299 K to fix the temporary shape. Finally, the member was placed in a hot water bath at 343 K and the free shape recovery process was observed.

5. Verification and discussion

5.1. Model parameter identification

The experimental measurements of the stress relaxation curves for SMP specimens shown in Fig. 3a were used to identify the shift factors and viscoelastic parameters of the matrix. The stress relaxation master curve at 323 K in Fig. 3b was constructed by shifting the stress relaxation curves at different temperatures along the logarithmic time axis based on the TTSP. The experimental values of the shift factor at various temperatures given in Fig. 3c were determined by the amount of translation of the corresponding stress relaxation curve along the logarithmic time axis. Eqs. (30) and (31) were used to fit the experimental measurements of shift factor to acquire fitted parameters such as C_1 , C_2 and $-AF_c/k_b$. Based on the pre-selected relaxation times $\tau_1 = 0.1$ s, $\tau_2 = 1$ s, $\tau_3 = 10$ s, $\tau_4 = 100$ s, $\tau_5 = 1000$ s and $\tau_6 = 10,000$ s, the equilibrium modulus E_0 and the relaxation modulus E_k ($k = 1, 2, \dots, 6$) of the matrix were obtained by fitting the stress relaxation master curve at 323 K using Eq. (24). The fitted curve is shown in Fig. 3d.

The proposed model takes into account the effect of thermal expansion in the finite element implementation, so the equivalent CTE of the composite must be determined in advance. The longitudinal CTE of the unidirectional composite is obtained by mixing rule (Gu et al., 2019)

$$\mu_1 = \frac{E_m \xi_m \mu_m + E_{f1} \xi_f \mu_{f1}}{E_m \xi_m + E_{f1} \xi_f} \quad (40)$$

where ξ_m and ξ_f are the volume fraction of matrix and fiber, respectively. The transverse CTE of the unidirectional composite is

$$\mu_2 = \mu_m (1 + \nu_m) \xi_m + \mu_{f2} (1 + \nu_f) \xi_f - \mu_1 (\nu_m \xi_m + \nu_f \xi_f) \quad (41)$$

The finalized model parameters are shown in Table 2.

The unidirectional fiber-reinforced composite is considered as a transversely isotropic material whose fourth-order stiffness tensor can be written in a Walpole's form with six parameters to simplify the tensor operations. The detailed operation rules of the Walpole's tensor are given in Supplementary material S2. The fourth-order Eshelby tensor \mathbb{S} and the interface-related fourth-order tensor \mathbb{R} need to be determined in advance before solving for the equivalent viscoelastic stiffness of the composite. For cylindrical fiber inclusions, the component of the fourth-order Eshelby tensor \mathbb{S} is (Pyo and Lee, 2010)

$$\mathbb{S}_{ijkl} = S_{IK}^{(1)} \delta_{ij} \delta_{kl} + S_{IJ}^{(2)} (\delta_{ik} \delta_{jl} + \delta_{il} \delta_{jk}) \quad (42)$$

where the specific expressions for $S_{IK}^{(1)}$ and $S_{IJ}^{(2)}$ are given in Supplementary material S3. The component of the fourth-order tensor \mathbb{R} is obtained by substituting Eq. (2) into Eq. (9) (Rao and Dai, 2017)

$$\mathbb{R}_{ijkl} = \alpha \mathbb{H}_{ijkl} + (\beta - \alpha) \mathbb{Q}_{ijkl} \quad (43)$$

For the cylindrical inclusion with a radius of a , the specific expressions for \mathbb{H}_{ijkl} and \mathbb{Q}_{ijkl} are given in Supplementary material S3.

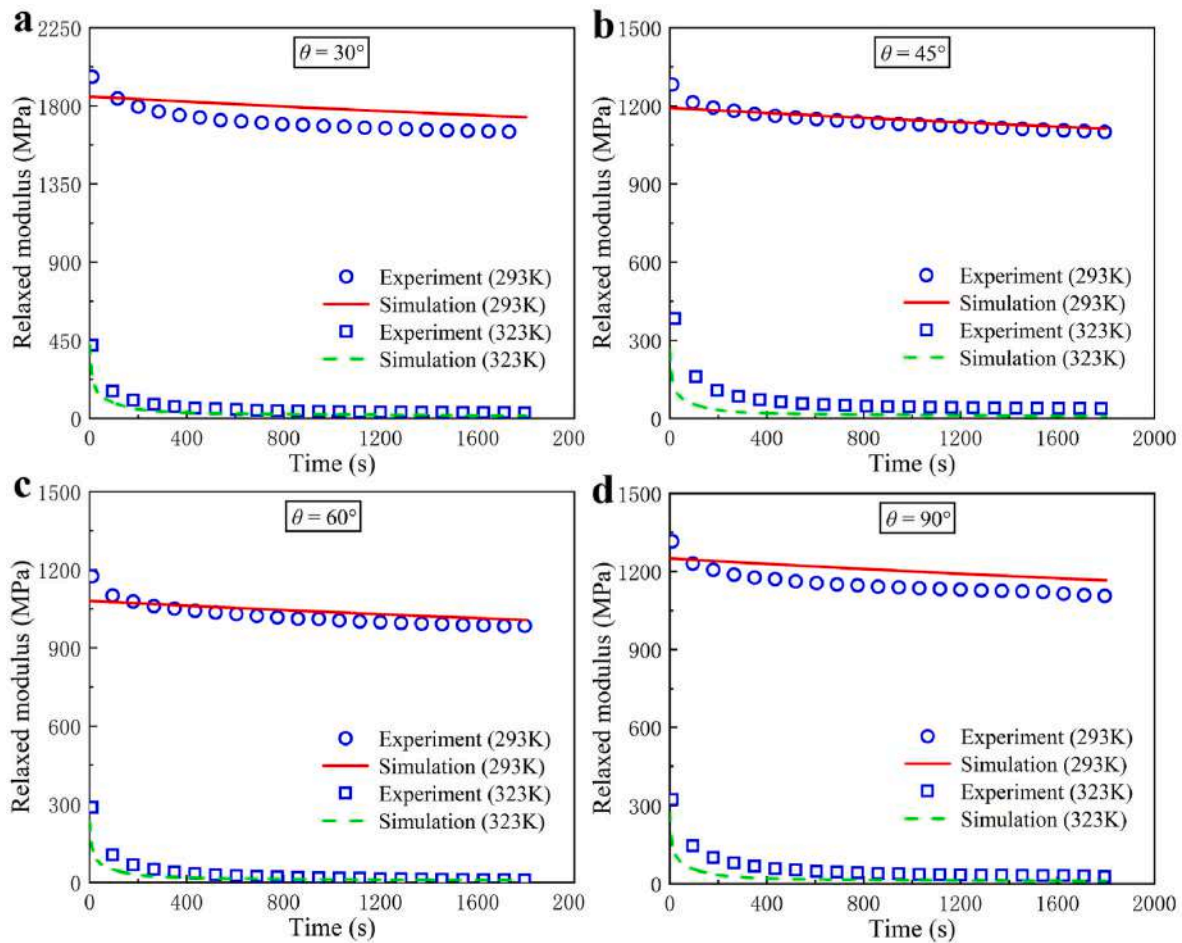


Fig. 8. Theoretical simulations and experimental measurements of the stress relaxation behavior of 4D printed SMPCs with a) $\theta = 30^\circ$, b) $\theta = 45^\circ$, c) $\theta = 60^\circ$ and d) $\theta = 90^\circ$ at different temperatures.

5.2. Parametric analysis

Taking the X_1 axis (the local coordinate system $O-X_1X_2X_3$ coincides with the global coordinate system $O-X_1X_2X_3$) as the symmetry axis of the cylindrical fiber inclusion, there are only five independent components in the equivalent stiffness matrix C_{IJ} of the transversely isotropic composite, which are C_{11} , C_{12} , C_{22} , C_{23} and C_{66} . Besides, the non-independent stiffness coefficient C_{44} can be calculated as $C_{44} = (C_{22} - C_{23})/2$. Fig. 4 presents the coupling effect of the interfacial damage parameters α and β on the equivalent stiffness coefficient of the viscoelastic composite at the moment $t = 0$ under a fixed fiber volume fraction $\xi_f = 12\%$, where both the horizontal axis (β) and the vertical axis (α) are presented in a logarithmic scale. It can be found that only the normal interfacial parameter β affects C_{11} and C_{12} . Conversely, for the stiffness coefficient C_{66} , only the tangential interfacial parameter α affects it. The equivalent stiffness coefficients depend on the magnitude of the interfacial parameter, and they decrease with increasing interfacial damage, as expected. Moreover, when the values of the interfacial parameters are in the range of 10^{-15} m/Pa to 10^{-13} m/Pa, slight parameter fluctuations will cause significant changes in the equivalent stiffness coefficients of the composite. For the stiffness coefficients C_{22} , C_{23} and C_{44} , the complex coupling effects of the two interfacial parameters are observed. The effect of the interfacial parameter α on the stiffness coefficients C_{22} and C_{23} is smaller compared to the interfacial parameter β .

The equivalent stiffness coefficients of the composite also depend on the fiber volume fraction for a specific interfacial damage parameter. Fig. 5 presents the predictions of the proposed model for the equivalent stiffness coefficients of the composite with specific tangential interfacial

parameters α and different fiber volume fractions. To simplify the analysis, only the cases of $\alpha = 10^{-15}$ m/Pa, 10^{-14} m/Pa and 10^{-13} m/Pa are presented here, and the normal interfacial parameter is set to $\beta = 0$. Fig. 5a and b shows that the interfacial parameter α has no impact on the stiffness coefficients C_{11} and C_{12} , which is consistent with the previous analysis. Fig. 5c–f exhibit the effects of the interfacial parameter α and fiber volume fraction on the stiffness coefficients C_{22} , C_{23} , C_{44} and C_{66} , respectively. The restricted domain is bounded by $\alpha = 0$ (no damage at the interface) and $\alpha = 1$ (tangential stiffness of the interface approaches 0). It can be observed from Fig. 5e and f that in the small interfacial damage regime (when α is small, e.g., $\alpha \leq 10^{-14}$ m/Pa), the equivalent stiffness coefficients C_{44} and C_{66} increase as the fiber volume fraction increases. However, as the interfacial damage increases (e.g., at $\alpha = 10^{-13}$ m/Pa), the equivalent stiffness coefficients C_{44} and C_{66} of the composite decrease as the fiber volume fraction increases, which is attributed to the extreme weakening of the load transfer between the fibers and the matrix due to increased interfacial damage.

5.3. Uniaxial tension and stress relaxation

In this section, based on the proposed micromechanical model, the uniaxial tensile and stress relaxation behavior of 4D printed SMPCs with various fiber lay-up angles ($\theta = 0^\circ, 30^\circ, 45^\circ, 60^\circ$ and 90°) at a fixed fiber volume fraction $\xi_f = 12\%$ and interfacial parameter $\alpha = 10^{-15}$ m/Pa were simulated. All simulations were run in the commercial finite element software ABAQUS, and the proposed thermo-viscoelastic model was implemented through the UMAT subroutine. In the simulation, the quadratic hexahedral element C3D20R with reduced integration was

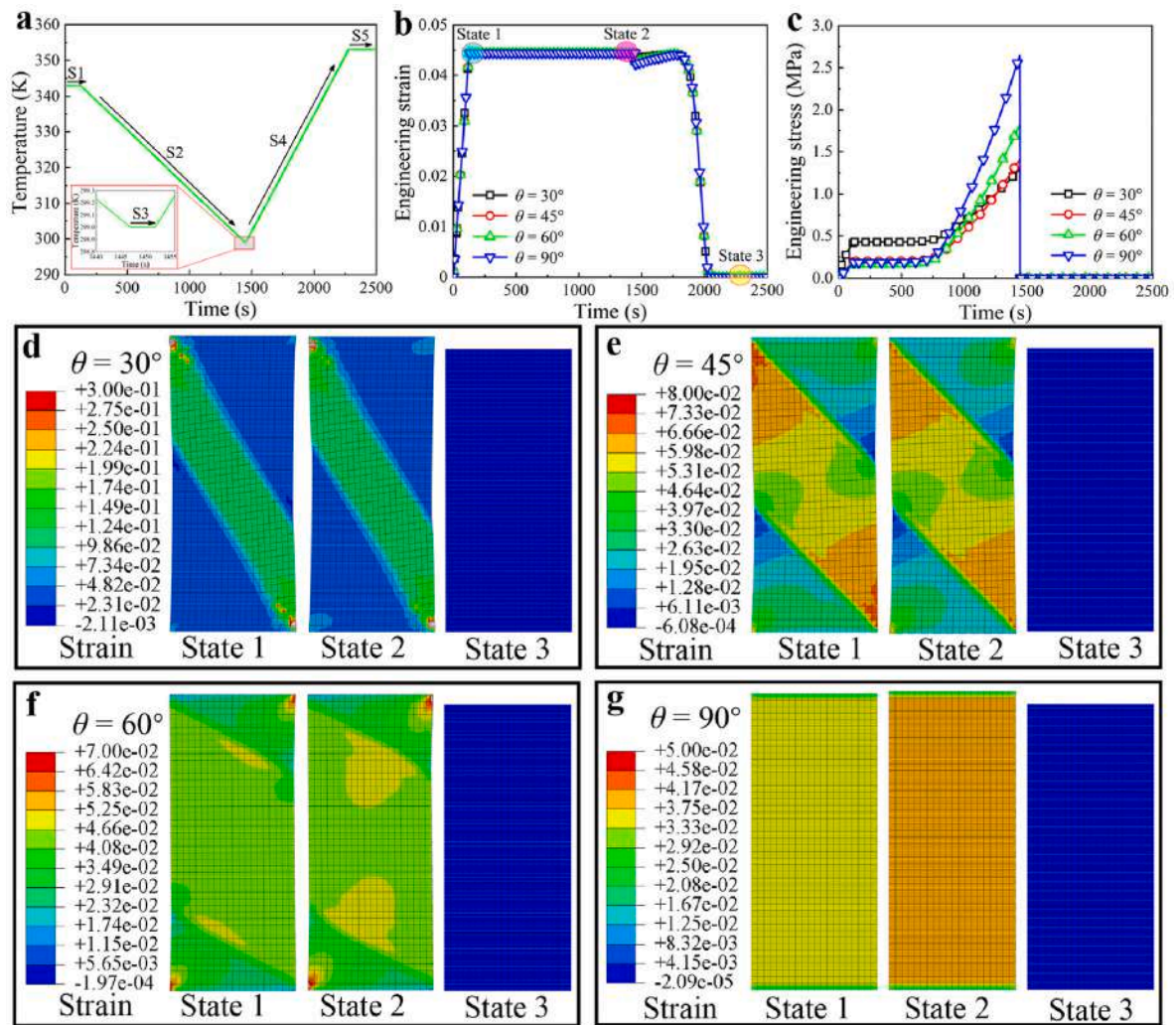


Fig. 9. Theoretical simulations of shape memory cycles for 4D printed SMPCs with various fiber lay-up angles. a) Time-temperature profile during shape memory cycles. b) Time-strain curves. c) Time-stress curves. Simulated deformed shapes and strain distribution clouds for the composites with d) $\theta = 30^\circ$, e) $\theta = 45^\circ$, f) $\theta = 60^\circ$ and g) $\theta = 90^\circ$ during shape memory cycles.

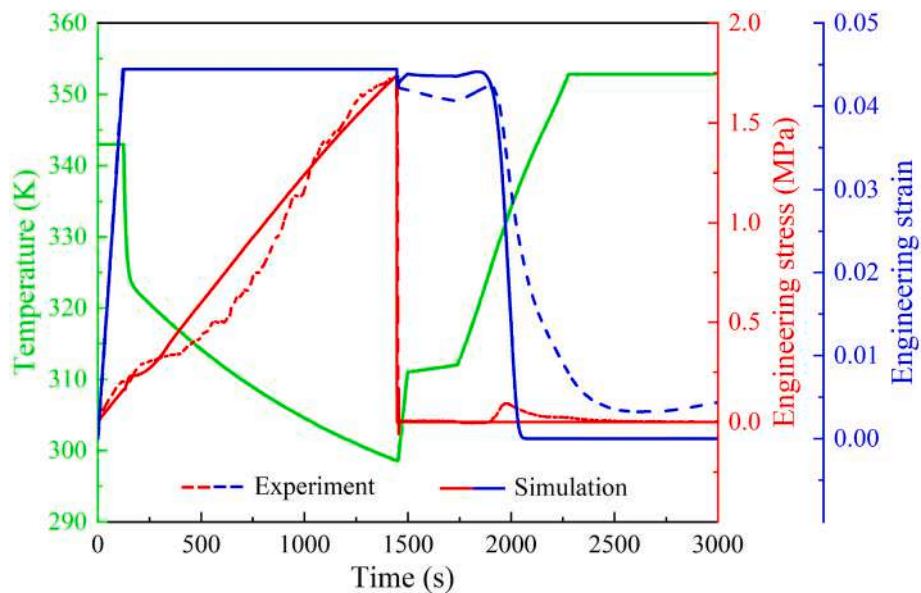


Fig. 10. Theoretical simulation and experimental measurement of the shape memory cycle for 4D printed composite with $\theta = 60^\circ$.

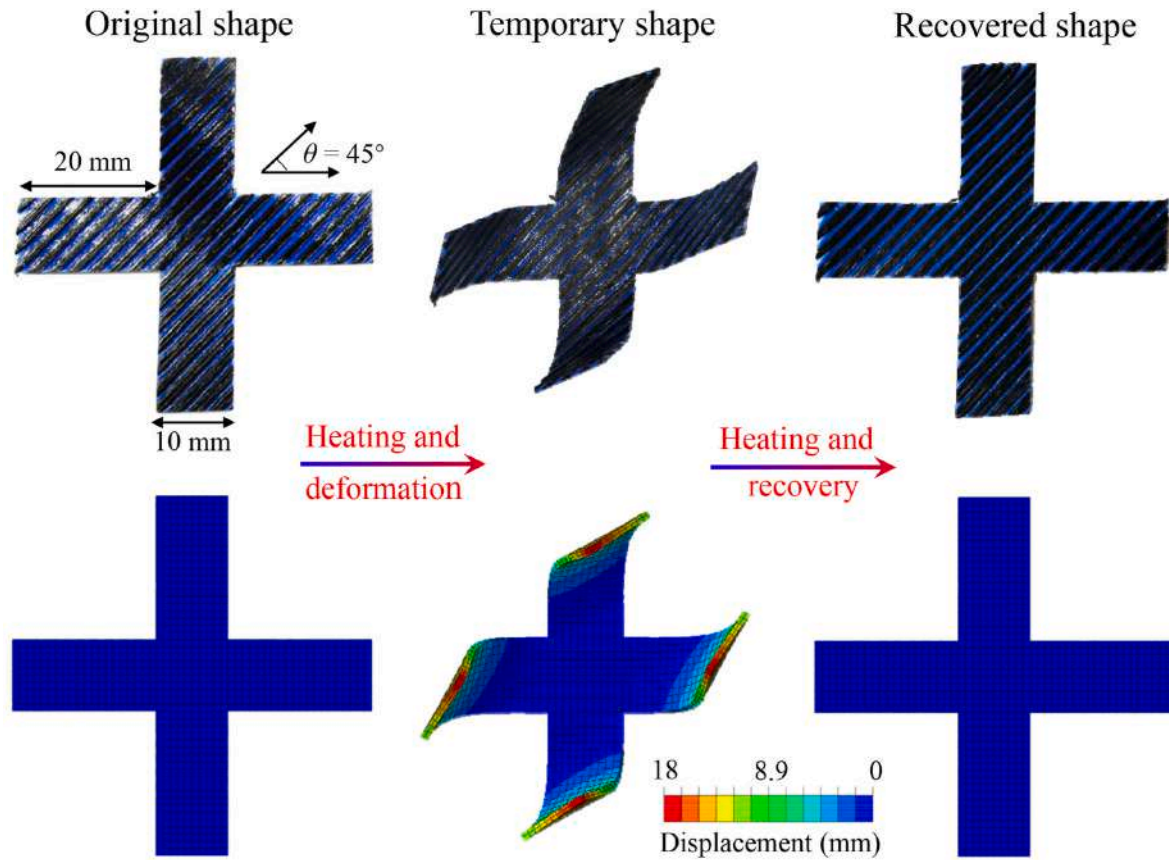


Fig. 11. The original shape, temporary shape and recovered shape of 4D printed cross-shaped SMPC member obtained by experiment and theoretical simulation during the shape memory cycle.

adopted, and the effect of different fiber lay-up angles was considered by defining a local coordinate system with an angle θ in the Ox_1x_2 plane with the global coordinate system.

From the finite element implementation process described in Section 3, the viscoelastic stiffness coefficients $C_{IJ,\infty}^{eq}$ and $C_{IJ,k}^{eq}$ of 4D printed SMPCs must be determined in advance, and the determined values are presented in Table 3. It is noteworthy that the interfacial effects between filaments, which are prone to occur in 3D printing processes represented by fused filament fabrication (FFF), are not included in the current discussion. However, since two interfacial damage parameters are incorporated, the proposed model can effectively simulate the interfacial effects between filaments if each filament is considered as a slender inclusion.

Fig. 6 presents the comparison between the uniaxial tensile experiment and the theoretical simulation of 4D printed SMPCs with $\theta = 0^\circ$, where the black dashed line represents the theoretical simulation. The theoretical simulation overestimates the stiffness of the composite, and this overestimation is attributed to the presence of fractures and distortions in the fiber bundles as well as matrix voids and interfacial defects caused by the 3D printing process. Here, we introduce a defect correction factor γ such that $\bar{C}_{IJ}^{eq} = \gamma C_{IJ}^{eq}$, where \bar{C}_{IJ}^{eq} is the corrected stiffness coefficient and $0 < \gamma \leq 1$ ($\gamma = 1$ means uncorrected). The red curve in Fig. 6 denotes the simulation of the engineering stress-strain curve for a correction factor $\gamma = 0.7$, which is in good agreement with the experiment. Therefore, the subsequent property predictions of 4D printed SMPCs with different fiber lay-up angles are obtained with a correction factor $\gamma = 0.7$.

Fig. 7 shows the comparison between theoretical simulations and experimental measurements of the tensile stress-strain curves of 4D printed SMPCs with various fiber lay-up angles at 293 K, from which it can be observed that the theoretical simulations agree well with the

experiments in the three cases of $\theta = 30^\circ$, 45° and 60° . However, Fig. 7 shows that the modified model with $\gamma = 0.7$ still overestimates the stiffness of 4D printed SMPCs at $\theta = 90^\circ$, which is attributed to the inherent defect caused by 3D printing process, i.e., poor transverse bonding of the components.

Stress relaxation is a typical mechanical phenomenon of viscoelastic polymers and their composites. Fig. 8 exhibits the comparison between the theoretical simulations and experimental measurements of the evolution curves of the stress relaxation modulus over time for 4D printed SMPCs with various θ at different temperatures. The proposed model demonstrates the satisfactory predictive capability for the relaxation behavior of 4D printed SMPCs. The modulus decays rapidly at the beginning of the relaxation period, and this decay gradually decreases with time. After a long time, the modulus converges to an equilibrium value. The proposed model exhibits a more accurate prediction of the equilibrium modulus after long-term relaxation compared to the initial relaxation modulus. This is probably attributed to the uncontrolled disturbances on the relaxation behavior of the specimen caused by the experimental fixture and environment at the beginning of relaxation.

5.4. Shape memory behavior

Fig. 9 presents theoretical simulations of shape memory cycles for 4D printed SMPCs with fiber lay-up angles θ of 30° , 45° , 60° and 90° . The temperature loading during the simulation is divided into five steps, following the time-temperature profile shown in Fig. 9a. Fig. 9b exhibits the time-strain profiles recorded during shape memory cycles, from which the typical strain free recovery process can be observed in the time interval from 1500 s to 2500 s, which demonstrates the effectiveness of the model in predicting the free shape recovery of SMPCs. Fig. 9c presents the time-stress curves of 4D printed SMPCs during shape

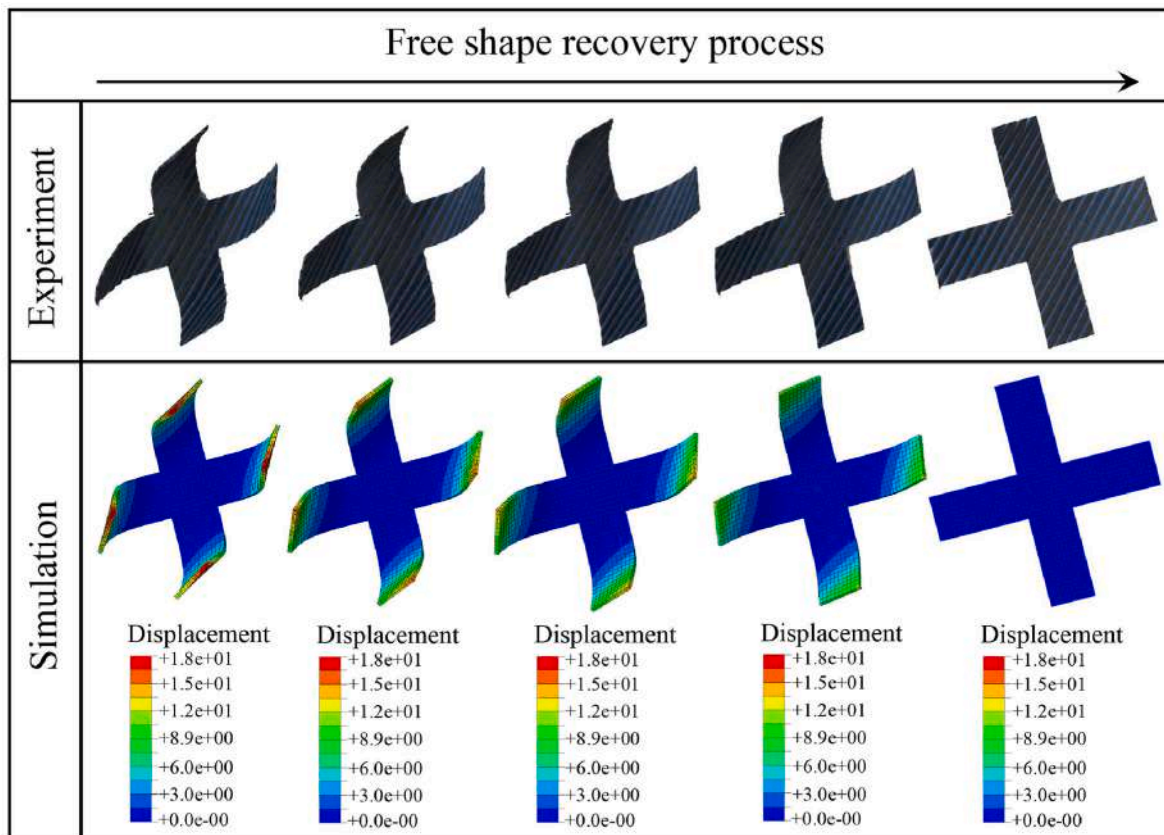


Fig. 12. Experiments and theoretical simulations for the free shape recovery process of 4D printed cross-shaped SMPC member.

memory cycles. In step 1 (S1), the maximum stresses for composites with $\theta = 30^\circ$, 45° , 60° , and 90° are 0.46 MPa, 0.20 MPa, 0.16 MPa, and 0.18 MPa, respectively. Obviously, the reinforcement effect of carbon fibers on the composite with $\theta = 30^\circ$ is the most significant. In step 2 (S2), the thermal contraction due to the decrease in temperature under the restrictive boundary conditions causes an increase in stress, and this trend of stress increase becomes more pronounced as the temperature decreases. In addition, the composite with $\theta = 30^\circ$ exhibits the least stress increase in step 2, which is attributed to the negative CTE of the carbon fiber in the longitudinal direction.

Fig. 9d–g respectively give the simulated deformed shapes of the composite with $\theta = 30^\circ$, 45° , 60° and 90° during shape memory cycles. The three states, namely State 1, State 2 and State 3, correspond to the moments marked in Fig. 9b. The local strain distribution in the specimen is directly related to the fiber lay-up angle as can be seen from strain clouds. For example, in Fig. 9d, it can be observed that the strain distribution of the composite specimen with $\theta = 30^\circ$ during loading presents a strip of approximately 30° from the tensile direction.

Fig. 10 shows the comparison between theoretical simulation and experiment of the shape memory cycle for 4D printed composite with $\theta = 60^\circ$. In the cooling phase (S2), the temperature change with time almost decays exponentially limited by the temperature-controlled chamber. The theoretical simulations can effectively predict the changing trend of stress and strain in the shape memory cycle. Of course, it can be found that one of the drawbacks of the proposed model is that the strain at the end of the shape memory cycle approaches zero (the shape recovery rate is close to 100%), which is not consistent with the experimental results. In the shape memory cycle test, the strain applied to the SMPC specimen in phase S1 was not fully recovered in phases S4 and S5, and this phenomenon was mainly attributed to the irreversible plastic deformation of the specimen. Besides, since the recovery force of the specimen during the shape recovery process was very low,

interactions such as friction between the fixture and the specimen would also affect the strain recovery. Therefore, the current model still needs to be improved in subsequent work to consider the plastic behavior of SMPCs, but it is not discussed in this article.

A 4D printed cross-shaped SMPC member was used to validate the ability of the proposed model to predict the shape memory behavior of complex composite structures. The original shape and dimensions of the member are shown in Fig. 11, and the fiber lay-up angle θ is 45° . At a temperature of 343 K, the four free branches of the cross-shaped member were rotated by a certain angle to obtain an inwardly rolled temporary shape, which was fixed by reducing the temperature. Then, the member with the temporary shape was placed in the environment of 343 K, which was able to return to a recovered shape close to the original shape.

Fig. 12 presents the experimental and simulated free recovery process of 4D printed cross-shaped SMPC member, from which a good agreement between the experimental and simulated deformations can be observed. Thus, it can be confirmed that the proposed model can effectively predict the shape memory behavior of complex composite components. The experimental and simulated shape recovery processes of 4D printed cross-shaped SMPC member are detailed in Supplementary Video S1 and Supplementary Video S2, respectively.

Supplementary data related to this article can be found at <https://doi.org/10.1016/j.mechmat.2022.104301>.

6. Conclusions

Although several constitutive models of SMPCs based on viscoelastic theory and thermodynamic free energy decomposition have been developed, there is still no constitutive model of multiphase SMPCs from the perspective of micromechanics has been proposed. In this work, we derived the equivalent stiffness tensor of the multiphase composite within a micromechanics framework based on Eshelby's equivalent

inclusion theory and Mori-Tanaka homogenization method, and the viscoelasticity of the SMP matrix was considered by the elastic-viscoelastic correspondence principle. A two-parameter interfacial spring model was employed to describe the interfacial damage between the inclusions and the matrix, and the effect of interfacial parameters and inclusion volume fraction on the initial equivalent stiffness coefficients of the unidirectional composite was analyzed.

The proposed viscoelastic model for SMPs was implemented in the commercial finite element software ABAQUS through the UMAT subroutine. 4D printed fiber-reinforced SMPs were used to validate the proposed model. Stress relaxation tests of PLA-based SMPs at multiple temperatures were conducted to determine the model parameters. Moreover, a series of tests including uniaxial tension, stress relaxation and shape memory cycling for 4D printed SMPs with various fiber lay-up angles were performed and compared with theoretical simulations. The results indicate that the theoretical model is able to effectively predict the uniaxial tensile curves, stress relaxation phenomena and shape memory behavior of 4D printed SMPs. Therefore, the theoretical framework and finite element implementation scheme presented in this paper may be useful for new mechanical research on viscoelastic composites including but not limited to 4D printing.

Author statement

Chengjun Zeng: Conceptualization, Visualization, Formal analysis, Writing – original draft, Writing - Reviewing & Editing. **Liwu Liu:** Methodology, Project administration, Writing - Reviewing & Editing. **Yunqiang Hu:** Investigation, Data curation, Writing - Reviewing & Editing. **Wenfeng Bian:** Visualization, Data curation, Writing - Reviewing & Editing. **Jinsong Leng:** Conceptualization, Project administration, Writing - Reviewing & Editing. **Yanju Liu:** Writing - Reviewing & Editing, Project administration, Supervision.

Declaration of competing interest

We declare that we do not have any commercial or associative interest that represents a conflict of interest in connection with the work submitted.

Acknowledgements

This work is supported by the Heilongjiang Touyan Innovation Team Program and the National Natural Science Foundation of China (Grant Nos. 11632005, 12072094 and 12172106).

Appendix A. Supplementary data

Supplementary data to this article can be found online at <https://doi.org/10.1016/j.mechmat.2022.104301>.

References

- Barbero, E.J., 2013. Finite Element Analysis of Composite Materials Using Abaqus. CRC press.
- Bennett, K.C., Luscher, D.J., Buechler, M.A., Yeager, J.D., 2018. A micromechanical framework and modified self-consistent homogenization scheme for the thermoelasticity of porous bonded-particle assemblies. *Int. J. Solid Struct.* 139–140, 224–237.
- Biswas, M.C., Chakraborty, S., Bhattacharjee, A., Mohammed, Z., 2021. 4D printing of shape memory materials for textiles: mechanism, mathematical modeling, and challenges. *Adv. Funct. Mater.* 31, 2100257.
- Dinzart, F., Sabar, H., 2017. New micromechanical modeling of the elastic behavior of composite materials with ellipsoidal reinforcements and imperfect interfaces. *Int. J. Solid Struct.* 108, 254–262.
- Elliott, L.V., Salzman, E.E., Greer, J.R., 2020. Stimuli responsive shape memory microarchitectures. *Adv. Funct. Mater.* 31, 2008380.
- Fang, C., Leng, J., Sun, H., Gu, J., 2018. A multi-branch thermoviscoelastic model based on fractional derivatives for free recovery behaviors of shape memory polymers. *Mech. Mater.* 120, 34–42.
- Ge, Q., Serjouei, A., Qi, H.J., Dunn, M.L., 2016. Thermomechanics of printed anisotropic shape memory elastomeric composites. *Int. J. Solid Struct.* 102–103, 186–199.
- Gomez-DelRio, A., Kwok, K., 2020. Stowage and Recovery of Thin-Ply Composite Deployable Structures. AIAA Scitech 2020 Forum.
- Gu, J., Leng, J., Sun, H., 2017. A constitutive model for amorphous shape memory polymers based on thermodynamics with internal state variables. *Mech. Mater.* 111, 1–14.
- Gu, J., Leng, J., Sun, H., Zeng, H., Cai, Z., 2019. Thermomechanical constitutive modeling of fiber reinforced shape memory polymer composites based on thermodynamics with internal state variables. *Mech. Mater.* 130, 9–19.
- Gu, J., Zhao, S., Zhang, X., Cai, Z., Sun, H., 2020. A hygro-thermo-mechanical constitutive model for hygrothermally activated shape memory polymers under finite deformations. *Mech. Mater.* 150, 103594.
- Hassanzadeh-Aghdam, M.K., Ansari, R., Mahmoodi, M.J., 2019. Thermo-mechanical properties of shape memory polymer nanocomposites reinforced by carbon nanotubes. *Mech. Mater.* 129, 80–98.
- Jarali, C.S., Madhusudan, M., Vidyashankar, S., Raja, S., 2018. A new micromechanics approach to the application of Eshelby's equivalent inclusion method in three phase composites with shape memory polymer matrix. *Compos. B Eng.* 152, 17–30.
- King, O., Constant, E., Weems, A.C., 2021. Shape memory poly(beta-hydroxythioether) foams for oil remediation in aquatic environments. *ACS Appl. Mater. Interfaces* 13, 20641–20652.
- Liu, Q., Lin, Y., Zong, Z., Sun, G., Li, Q., 2013. Lightweight design of carbon twill weave fabric composite body structure for electric vehicle. *Compos. Struct.* 97, 231–238.
- Liu, W., Bian, L., 2019. A new energy-based effective strain theory for mechanical properties of multiphase composites. *Eur. J. Mech. Solid.* 76, 279–289.
- Liu, Y., Gall, K., Dunn, M.L., Greenberg, A.R., Diani, J., 2006. Thermomechanics of shape memory polymers: uniaxial experiments and constitutive modeling. *Int. J. Plast.* 22, 279–313.
- Mao, Y., Chen, F., Hou, S., Qi, H.J., Yu, K., 2019. A viscoelastic model for hydrothermally activated malleable covalent network polymer and its application in shape memory analysis. *J. Mech. Phys. Solid.* 127, 239–265.
- Mao, Y., Robertson, J.M., Mu, X., Mather, P.T., Jerry Qi, H., 2015. Thermoviscoelastic behaviors of anisotropic shape memory elastomeric composites for cold programmed non-affine shape change. *J. Mech. Phys. Solid.* 85, 219–244.
- Nguyen, T., Jerryqi, H., Castro, F., Long, K., 2008. A thermoviscoelastic model for amorphous shape memory polymers: incorporating structural and stress relaxation. *J. Mech. Phys. Solid.* 56, 2792–2814.
- Pyo, S.H., Lee, H.K., 2010. An elastoplastic damage model for metal matrix composites considering progressive imperfect interface under transverse loading. *Int. J. Plast.* 26, 25–41.
- Qi, H.J., Nguyen, T.D., Castro, F., Yakacki, C.M., Shandas, R., 2008. Finite deformation thermo-mechanical behavior of thermally induced shape memory polymers. *J. Mech. Phys. Solid.* 56, 1730–1751.
- Qu, J., 1993. Eshelby tensor for an elastic inclusion with slightly weakened interface. *J. Appl. Mech.* 60 (4), 1048–1050.
- Rao, Y.-N., Dai, H.-L., 2017. Micromechanics-based thermo-viscoelastic properties prediction of fiber reinforced polymers with graded interphases and slightly weakened interfaces. *Compos. Struct.* 168, 440–455.
- Saadat, F., Birman, V., Thomopoulos, S., Genin, G.M., 2015. Effective elastic properties of a composite containing multiple types of anisotropic ellipsoidal inclusions, with the application to the attachment of tendon to bone. *J. Mech. Phys. Solid.* 82, 367–377.
- Su, X., Wang, Y., Peng, X., 2020. An anisotropic visco-hyperelastic model for thermally-actuated shape memory polymer-based woven fabric-reinforced composites. *Int. J. Plast.* 129, 102697.
- Tan, Q., Liu, L., Liu, Y., Leng, J., 2014. Thermal mechanical constitutive model of fiber reinforced shape memory polymer composite: based on bridging model. *Compos. Part A Appl. Sci. Manuf.* 64, 132–138.
- Xia, Y., He, Y., Zhang, F., Liu, Y., Leng, J., 2021. A review of shape memory polymers and composites: mechanisms, materials, and applications. *Adv. Mater.* 33, e2000713.
- Xin, X., Liu, L., Liu, Y., Leng, J., 2021. Prediction of effective thermomechanical behavior of shape memory polymer composite with micro-damage interface. *Compos. Commun.* 25, 100727.
- Yapa Hamillage, M., Leung, C., Kwok, K., 2022. Viscoelastic modeling and characterization of thin-ply composite laminates. *Compos. Struct.* 280, 114901.
- Yu, K., Xie, T., Leng, J., Ding, Y., Qi, H.J., 2012. Mechanisms of multi-shape memory effects and associated energy release in shape memory polymers. *Soft Matter* 8, 5687.
- Yu, K., McClung, A.J.W., Tandon, G.P., Baur, J.W., Jerry Qi, H., 2014a. A thermomechanical constitutive model for an epoxy based shape memory polymer and its parameter identifications. *Mech. Time-Dependent Mater.* 18, 453–474.
- Yu, K., Ge, Q., Qi, H.J., 2014b. Reduced time as a unified parameter determining fixity and free recovery of shape memory polymers. *Nat. Commun.* 5, 3066.
- Zeng, C., Liu, L., Bian, W., Leng, J., Liu, Y., 2021. Compression behavior and energy absorption of 3D printed continuous fiber reinforced composite honeycomb structures with shape memory effects. *Addit. Manuf.* 38, 101842.
- Zeng, C., Liu, L., Bian, W., Leng, J., Liu, Y., 2022. Temperature-dependent mechanical response of 4D printed composite lattice structures reinforced by continuous fiber. *Compos. Struct.* 280, 114952.
- Zhang, L., Lin, Q., Chen, F., Zhang, Y., Yin, H., 2020. Micromechanical modeling and experimental characterization for the elastoplastic behavior of a functionally graded material. *Int. J. Solid Struct.* 206, 370–382.
- Zhang, W., Zhang, F., Lan, X., Leng, J., Wu, A.S., Bryson, T.M., Cotton, C., Gu, B., Sun, B., Chou, T.-W., 2018. Shape memory behavior and recovery force of 4D printed textile functional composites. *Compos. Sci. Technol.* 160, 224–230.

- Zhao, W., Liu, L., Leng, J., Liu, Y., 2019. Thermo-mechanical behavior prediction of particulate reinforced shape memory polymer composite. *Compos. B Eng.* 179, 107455.
- Zhao, W., Liu, L., Leng, J., Liu, Y., 2020. Thermo-mechanical behavior prediction of shape memory polymer based on the multiplicative decomposition of the deformation gradient. *Mech. Mater.* 143, 103263.
- Zobeiry, N., Malek, S., Vaziri, R., Poursartip, A., 2016. A differential approach to finite element modelling of isotropic and transversely isotropic viscoelastic materials. *Mech. Mater.* 97, 76–91.
- Zocher, M., Groves, S., Allen, D., 1997. A three-dimensional finite element formulation for thermoviscoelastic orthotropic media. *Int. J. Numer. Methods Eng.* 40, 2267–2288.